




Cite this: *Chem. Sci.*, 2025, 16, 21542 All publication charges for this article have been paid for by the Royal Society of Chemistry

# Supercritical CO<sub>2</sub>-modulated phase transition in CaSnO<sub>3</sub> from orthorhombic to cubic symmetry for room-temperature ferromagnetism

Lei Xu,<sup>a</sup> Qun Xu <sup>\*a</sup> and Buxing Han <sup>b</sup>

The advancement of nanotechnology has enabled magnetic nanomaterials to exhibit remarkable potential and application value in medicine, transportation, information storage, and spintronics owing to their unique physicochemical properties. In this study, supercritical carbon dioxide (SC CO<sub>2</sub>) was used to successfully induce room-temperature ferromagnetism in CaSnO<sub>3</sub> without magnetic element doping, achieving a maximum saturation magnetization of 0.0727 emu g<sup>-1</sup> at 16 MPa. The SC CO<sub>2</sub> treatment introduced lattice-scale defects, releasing residual force within distorted SnO<sub>6</sub> octahedra, which led to the suppression of structural distortion and drove a structural phase transition from orthorhombic to cubic. Additionally, the enhanced symmetry was accompanied by anisotropic lattice expansion and tensile strain, which thermodynamically lowered the oxygen vacancy formation energy, thereby kinetically driving the creation of more defects. This disrupted the intrinsic antiferromagnetic order and significantly enhanced ferromagnetism. This work elucidates a defect-strain synergy mechanism for tuning material magnetic order, distinguishing it from conventional stoichiometric doping strategies and highlighting the critical role of SC CO<sub>2</sub> in material modification.

Received 2nd July 2025

Accepted 28th September 2025

DOI: 10.1039/d5sc04873g

rsc.li/chemical-science

## Introduction

With the advancement of nanotechnology, magnetic nanomaterials have shown great potential and application value in areas such as medicine,<sup>1</sup> transportation,<sup>2</sup> information storage<sup>3</sup> and spintronics<sup>4–7</sup> due to their unique physicochemical properties. Room-temperature ferromagnetic materials offer great potential for a variety of advanced technology applications, as well as new possibilities for the next generation of low-power, high-density electronic and information storage devices.<sup>8</sup> Perovskites are excellent candidates for ferromagnetic materials, benefiting from their tunable crystal structures<sup>9</sup> and good electron correlation properties,<sup>10</sup> as well as a strong spin–orbit coupling effect.<sup>11</sup> Among the plethora of perovskite materials, alkaline earth stannate CaSnO<sub>3</sub> has attracted great interest from many researchers because of its wide band gap,<sup>12</sup> high melting point,<sup>13</sup> and excellent optical<sup>14</sup> and semiconductor properties.<sup>12</sup> However, comparatively limited research has been conducted on the ferromagnetism of CaSnO<sub>3</sub>. The CaSnO<sub>3</sub> perovskite is composed of octahedral SnO<sub>6</sub> and its vertices are linked to each other by mutual sharing of oxygen.<sup>15</sup> In the ideal orthorhombic structure (*Pbnm*) of bulk CaSnO<sub>3</sub>, the Sn<sup>4+</sup> ion occupies the center of the oxygen octahedron. Due to its d<sup>10</sup> electron

configuration, Sn<sup>4+</sup> has no local magnetic moment, ruling out the possibility of ferromagnetism at room temperature.<sup>16</sup>

In the existing studies, the modulation of the ferromagnetism of CaSnO<sub>3</sub> materials is mainly through elemental doping, and there is no focus on their intrinsic ferromagnetism.<sup>17</sup> Aadil Ahmad Bhat *et al.*<sup>18</sup> synthesized and tested Mn and Ce doped CaSnO<sub>3</sub> nanomaterials using a hydrothermal method. The doping modified the internal chemical environment of the materials, and the diamagnetic CaSnO<sub>3</sub> host perovskite transformed into a ferromagnetic material. Therefore, is there a new method that can effectively modulate the internal structure and intrinsic ferromagnetism of CaSnO<sub>3</sub> without introducing other elements? In our previous work, SC CO<sub>2</sub> has been used to modulate the selective breaking of covalent bonds in CaTiO<sub>3</sub>,<sup>19</sup> thereby exposing a specific crystalline surface that exhibits excellent room-temperature ferromagnetism. In addition, it was found that SC CO<sub>2</sub> facilitates the conversion of external pressure into chemical pressure inside BaZrO<sub>3</sub>,<sup>20</sup> changing the chemical environment of BaZrO<sub>3</sub> and thus, effectively modulating its ferromagnetic properties. These endeavors capitalize on the distinctive physicochemical characteristics exhibited by supercritical CO<sub>2</sub>,<sup>21–26</sup> including exceptional diffusivity, negligible surface tension, and adjustable solvation power,<sup>27</sup> which enable its selective penetration into crystalline matrices to facilitate defect generation and strain field redistribution while preserving the overall structural integrity of the crystalline framework.

<sup>a</sup>Henan Institute of Advanced Technology, Zhengzhou University, Zhengzhou 450003, P. R. China. E-mail: qunxu@zzu.edu.cn

<sup>b</sup>Institute of Chemistry, Chinese Academy of Science, Beijing 100080, P. R. China



In this study, an alternative strategy to conventional elemental doping is proposed, in which SC CO<sub>2</sub> is utilized to induce lattice-scale defects in CaSnO<sub>3</sub>, thereby effectively releasing residual force within distorted SnO<sub>6</sub> octahedra and driving a structural phase transition from orthorhombic to cubic symmetry. In addition, the symmetry elevation induces pronounced anisotropic lattice expansion and tensile strain, which thermodynamically lowers the oxygen vacancy formation energy, thereby kinetically driving the creation of more defects, and ultimately induces the antiferromagnetic CaSnO<sub>3</sub> to exhibit room-temperature ferromagnetism after SC CO<sub>2</sub> treatment.

## Results and discussion

### Structural characterization of CaSnO<sub>3</sub>

The structures of the CaSnO<sub>3</sub> nanosheets prepared under different SC CO<sub>2</sub> pressures were characterized by X-ray diffraction (XRD). Fig. 1a illustrates the XRD patterns of CaSnO<sub>3</sub> containing labeled diffraction peak sites. Analysis of these peaks using Jade software confirmed that the untreated sample (bulk) exhibited an orthorhombic phase (PDF card no. 77-1797, space group *Pbnm*).<sup>28</sup> Unexpectedly, the SC CO<sub>2</sub>-treated CaSnO<sub>3</sub> exhibited a coexistence of *Pbnm* and *Fm3m* phases.<sup>29</sup> During the process of conversion from *Pbnm* to *Fm3m*, the crystal structure and cell parameters of CaSnO<sub>3</sub> change dramatically: the symmetry of the crystal is increased, and the bond angle between its two SnO<sub>6</sub> octahedra becomes larger (from 148° to 180°). This was attributed to the anisotropic expansion of the orthorhombic lattice due to SC CO<sub>2</sub> penetration (see Table S1, SI), which lowers the phase transition energy barrier and induces the emergence of new cubic phases.<sup>30</sup> Specifically, the analysis focused on three characteristic peaks, (110), (112), and (004). As shown in Fig. 1b–d, the diffraction peak of CaSnO<sub>3</sub> after SC CO<sub>2</sub> treatment shifted towards lower angles. When the pressure of SC CO<sub>2</sub> reaches 16 MPa, the three characteristic peaks are most clearly shifted to a lower angle, providing key evidence for the increased lattice spacing originating from the strain effect due to the SC CO<sub>2</sub> treatment.

To further confirm the changes in the crystal structure of the samples after SC CO<sub>2</sub> treatment, the XRD diffraction data were refined using Rietveld structural refinement. This analysis was conducted to assess the alterations in cell parameters and validate the formation of the new phase. The bulk CaSnO<sub>3</sub> crystals usually tend to form orthorhombic phases due to the difficulty in releasing structural stress. When the SC CO<sub>2</sub> pressure was increased from 14 to 16 MPa, it kinetically facilitated the increase of oxygen vacancy defects inside the crystal and prompted the release of lattice stresses around the defects, and the content of the cubic phase CaSnO<sub>3</sub> was changed from 19% to 32% (see Fig. 1e and S1, SI). However, further pressure increase to 18 MPa unexpectedly reduced the cubic phase content to 17% (see Fig. S1, SI). This reversal could potentially originate from excessive SC CO<sub>2</sub> infiltration, which may have driven the elastic strain energy of the cubic phase beyond its thermodynamic stability threshold. Such over penetration likely facilitated amorphous phase formation through destabilization of the crystalline lattice.

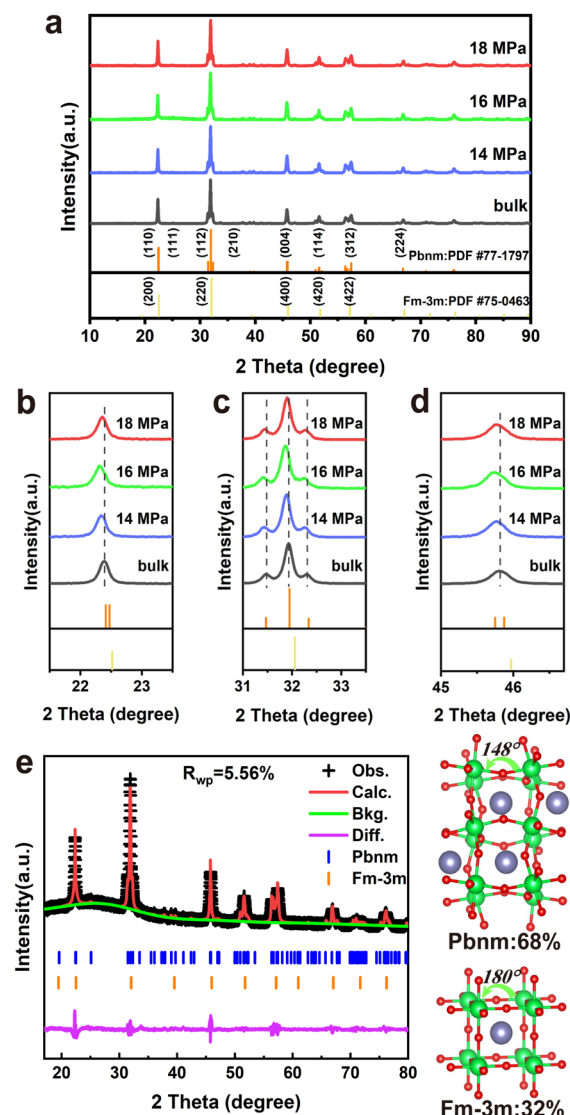


Fig. 1 Characterizations of CaSnO<sub>3</sub> treated under different SC CO<sub>2</sub> pressures. (a) Survey characterization of XRD. Enlarged views of some planes: (b) (110) plane, (c) (112) plane, and (d) (004) plane. (e) The Rietveld structure refinement and structure under 16 MPa.

To characterize the micromorphology of the prepared CaSnO<sub>3</sub> with different pressures of SC CO<sub>2</sub>, high-resolution transmission electron microscopy (HRTEM) is used. Fig. 2a presents the TEM image of the untreated sample, revealing a well-defined orthorhombic structure. This observation is further corroborated by the SAED pattern shown in Fig. 2e, which exhibits distinct diffraction spots corresponding to the (210) and (004) crystallographic planes. These characteristic features are consistent with the *Pbnm* phase structure of CaSnO<sub>3</sub>, confirming the crystallographic orientation and phase purity in the absence of SC CO<sub>2</sub> treatment. Under a 14 MPa CO<sub>2</sub> pressure, the TEM analysis in Fig. 2b revealed the structural coexistence of both orthorhombic and cubic CaSnO<sub>3</sub> phases, with the corresponding SAED pattern in Fig. 2f displaying dual diffraction arrays. Crystallographic indexing unambiguously assigned these diffraction features to the *Pbnm* orthorhombic

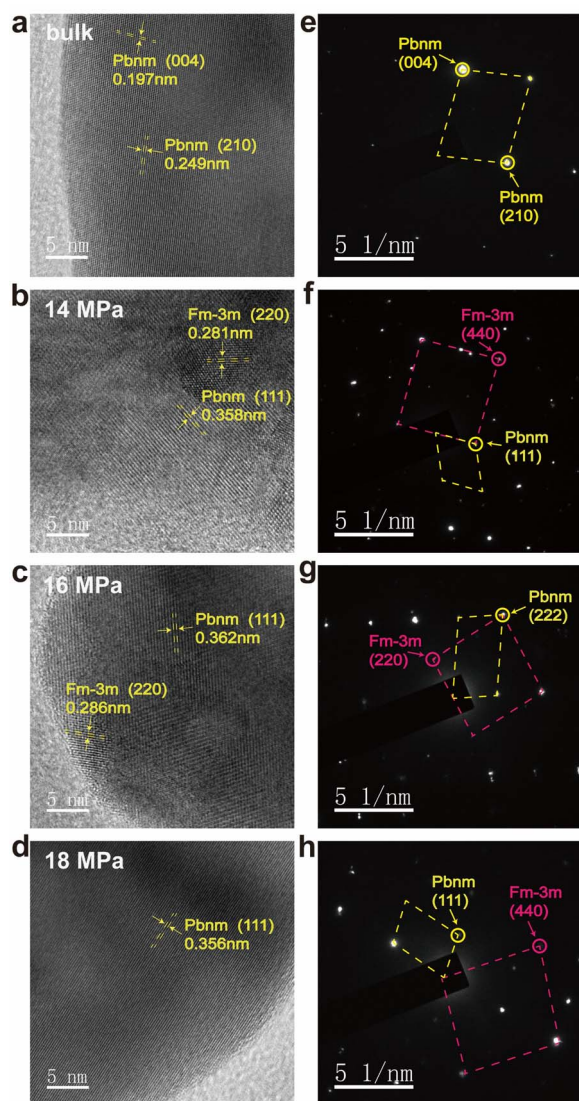


Fig. 2 Characterizations of CaSnO<sub>3</sub> treated under different SC CO<sub>2</sub> pressures. (a–d) High-magnification TEM images of the bulk material and that under pressures of 14, 16 and 18 MPa. (e–h) SAED diffraction patterns of CaSnO<sub>3</sub> samples of the bulk material and those under pressures of 14, 16 and 18 MPa.

system and *Fm* $\bar{3}$ *m* cubic system. Similarly, Fig. 2c and g show a pair of TEM images and SAED diffraction pattern corresponding to treatment with a 16 MPa CO<sub>2</sub> pressure, exhibiting characteristic lattice spacings of 0.362 nm and 0.286 nm corresponding to the orthorhombic (111) and cubic (220) planes. Compared to standard CaSnO<sub>3</sub> PDF cards (*Pbnm* phase: PDF#77-1797; *Fm* $\bar{3}$ *m* phase: PDF#75-0463), both planes show maximum lattice stretching at 16 MPa, indicating that SC CO<sub>2</sub> pressure-driven structural changes occur preferentially along these crystallographic orientations. However, when the CO<sub>2</sub> pressure increases from 16 to 18 MPa, the cubic phase CaSnO<sub>3</sub> is difficult to observe in the TEM image presented in Fig. 2d. This phenomenon likely stems from the enhanced density and solvation power of SC CO<sub>2</sub> under elevated pressures, which intensifies interactions with the material. The cubic CaSnO<sub>3</sub>

phase, characterized by its higher crystallographic symmetry and expanded oxygen octahedral network, exhibits heightened susceptibility to structural disordering. These features lower the Gibbs free energy barriers for amorphous nucleation, facilitating phase transformation kinetics, thereby inducing localized amorphization within cubic phase domains (see Fig. S2, SI). The diminished long-range crystallographic coherence becomes challenging to resolve *via* TEM imaging, while short-range ordered atomic configurations remain detectable through characteristic SAED pattern in Fig. 2h, reflecting residual structural correlations at sub-nanometer scales.

Additionally, scanning electron microscopy (SEM) and energy dispersive spectroscopy (EDS) were employed to examine the surface morphology and elemental distribution of CaSnO<sub>3</sub> before and after treatment (see Fig. S3 and S4, SI). Significant changes in surface morphology were observed following SC CO<sub>2</sub> treatment. EDS mapping further revealed a decrease in oxygen content with increasing pressure, providing direct evidence for the increased oxygen vacancy concentration, which is attributable to the pressure-induced penetration of SC CO<sub>2</sub>, which progressively increased lattice defects and induced surface amorphization.

Internal structures and molecular vibrations of CaSnO<sub>3</sub> treated under different SC CO<sub>2</sub> pressures were investigated using Raman spectroscopy, as shown in Fig. 3a. Group theoretical analysis reveals that the CaSnO<sub>3</sub> bulk material with the *Pbnm* space group exhibits 24 Raman-active modes ( $\Gamma$  Raman =  $7A_g + 5B_{1g} + 7B_{2g} + 5B_{3g}$ ).<sup>31</sup> The samples all show three characteristic peaks in common, with spectral bands in the range 164–227 cm<sup>−1</sup> (*B*<sub>2g</sub>) possibly related to octahedral rotation of

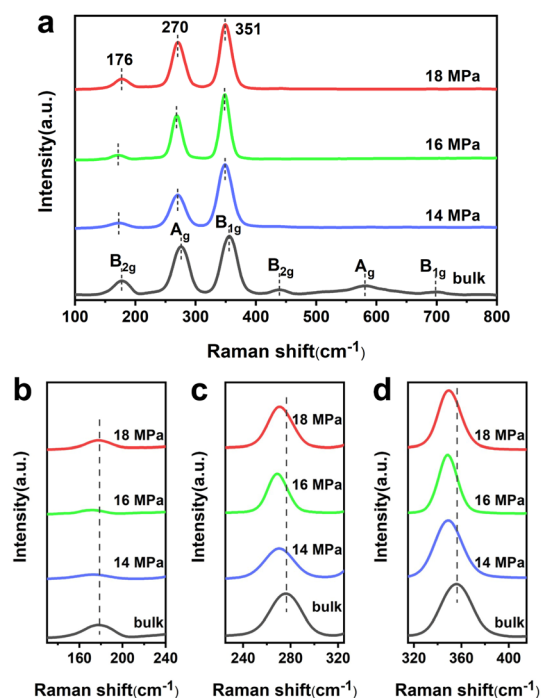


Fig. 3 Characterization of CaSnO<sub>3</sub> treated with different pressures of SC CO<sub>2</sub>. (a) Raman spectra. Enlarged views of some characteristic peaks: (b) 176 cm<sup>−1</sup>, (c) 270 cm<sup>−1</sup>, and (d) 351 cm<sup>−1</sup>.



oxygen,<sup>32</sup> and bands near  $270\text{ cm}^{-1}$  ( $A_g$ ) and  $351\text{ cm}^{-1}$  ( $B_{1g}$ ) related to shifts in Ca and O.<sup>32</sup>

In particular, the bands associated with the bending or stretching of Sn–O bonds near  $420\text{ cm}^{-1}$  ( $B_{2g}$ ) and the twisting of  $\text{SnO}_6$  octahedra near  $580$  ( $A_g$ ) and  $695\text{ cm}^{-1}$  ( $B_{1g}$ )<sup>17</sup> disappeared after treatment with SC  $\text{CO}_2$ . This arises from the simplicity of the vibrational modes and activity suppression due to the elevated symmetry of the crystal.<sup>33</sup> The orthorhombic phase has multiple structural distortions, such as tilting of the oxygen octahedra and cation displacements. These distortions induce Brillouin zone folding effects that generate multiple Raman-active modes. However, the restoration of cubic symmetry eliminates these distortions, causing originally split vibrational modes (e.g.  $B_{2g}/B_{1g}/A_g$ ) to merge into higher-symmetry representations through mode simplification, resulting in the disappearance of some of the peaks. Specifically, the Sn–O bond bending/stretching and octahedral twisting modes become Raman-inactive under cubic symmetry constraints. Consequently, the disappearance of specific peaks in the  $400\text{--}800\text{ cm}^{-1}$  range reflects a fundamental symmetry shift in lattice dynamics during the orthorhombic to cubic phase transition. In addition, the surviving Raman peaks in Fig. 3b–d exhibit systematic redshifts after SC  $\text{CO}_2$  treatment. The  $B_{2g}$  peak shift originates from symmetry recovery in oxygen octahedra, where the elimination of rotational distortions increases Sn–O bond lengths and reduces vibrational force constants. The  $A_g$  and  $B_{1g}$  peak displacements arise from local polarization suppression; cubic symmetry constraints force  $\text{Ca}^{2+}$  ions back to high-symmetry positions, annihilating displacement-dependent vibrational modes while weakening residual Ca–O coupling, leading to coordinated frequency downshift.

X-ray photoelectron spectroscopy (XPS) was employed to characterize the oxidation states of tin and oxygen. The total XPS characterization (see Fig. S5, SI) indicates that no other magnetic impurities are present in  $\text{CaSnO}_3$ . Fig. 4a illustrates that the XPS of O 1s in  $\text{CaSnO}_3$  can be divided into three peaks with binding energies of 529.9, 531.7, and 533.6 eV. These peaks were assigned to the lattice oxygen  $\text{O}_L$  (Sn–O–Sn and Ca–O), the oxygen vacancy  $\text{O}_V$ , and oxygen adsorption  $\text{O}_A$ , respectively.<sup>34</sup> A notable transformation is observed in comparison to the bulk material, and the percentage of oxygen vacancies increases from 36% to 40%, 48%, and 39%, following SC  $\text{CO}_2$  treatment at different pressures. Fig. 4b illustrates that the XPS spectra of Sn exhibit two principal peaks, which correspond to  $\text{Sn } 3d_{5/2}$  and  $\text{Sn } 3d_{3/2}$  with binding energies of 486.4 and 494.8 eV, respectively. A shift of the two main peaks is observed in the samples treated with SC  $\text{CO}_2$ , so the emergence of two additional peaks at low binding energies is evident, which can be attributed to  $\text{Sn}^{3+}$ . Furthermore, an increase in  $\text{CO}_2$  pressure resulted in a corresponding change in  $\text{Sn}^{3+}$  content. The observed phenomenon originates from the chemical reaction within  $\text{CaSnO}_3$ , leading to the simultaneous formation of  $\text{Sn}^{3+}$  species and  $\text{O}_V$ . Specifically, each  $\text{O}_V$  formation corresponds to the reduction of two adjacent  $\text{Sn}^{4+}$  cations to  $\text{Sn}^{3+}$  through charge compensation mechanisms.

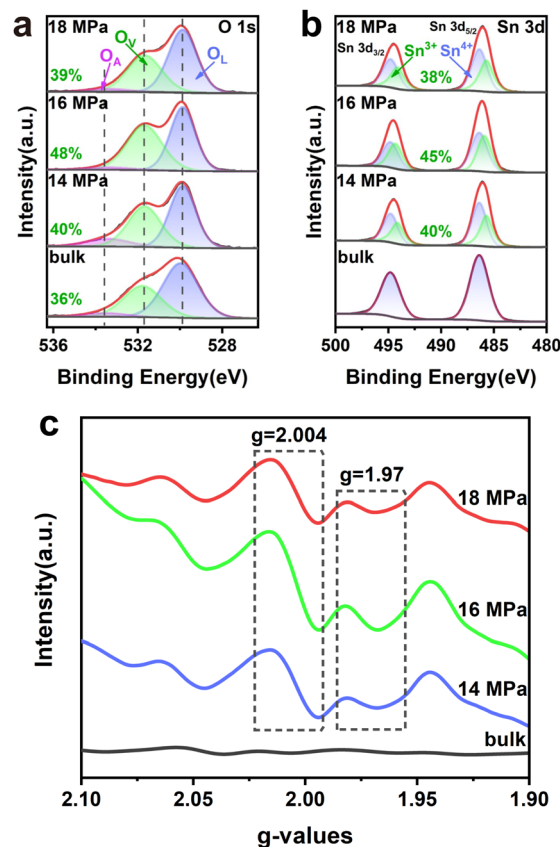


Fig. 4 XPS characterization under different SC  $\text{CO}_2$  pressures. (a) O 1s XPS. The percentage contents in (a) represent  $\text{O}_V$ . (b) Sn 3d XPS. The percentage contents in (b) represent  $\text{Sn}^{3+}$ . (c) Electron paramagnetic resonance (EPR) spectra.

The EPR spectra are illustrated in Fig. 4c. The samples treated with SC  $\text{CO}_2$  exhibit pronounced signals at  $g = 2.004$  and  $g = 1.97$ , which corroborate the generation of  $\text{O}_V$ <sup>35</sup> and  $\text{Sn}^{3+}$ .<sup>36</sup> The signal with  $g = 2.004$  can be assigned to  $\text{O}_V$ , and the other signal at  $g = 1.97$  is attributed to  $\text{Sn}^{3+}$ . As illustrated in Fig. 4c, the intensities of the characteristic peaks corresponding to  $\text{O}_V$  and  $\text{Sn}^{3+}$  show a significant increase when the  $\text{CO}_2$  pressure is increased to 16 MPa, and then show a period of weakening as the  $\text{CO}_2$  pressure increases to 18 MPa. This phenomenon can be attributed to the fact that increased pressure in the range of 14–16 MPa enhances the penetration of SC  $\text{CO}_2$ , which intensifies the disruption of Sn–O bonds and promotes the formation of  $\text{O}_V$  and  $\text{Sn}^{3+}$ . Additionally, as the  $\text{CO}_2$  pressure continues to increase, it promotes the formation of structurally disordered amorphous phases, leading to the migration or annihilation of oxygen vacancies and affecting the stability of  $\text{Sn}^{3+}$ . This trend is consistent with the XPS results.

### Magnetic properties

Fig. 5a and b show the room temperature M–H plots of  $\text{CaSnO}_3$  samples before and after SC  $\text{CO}_2$  treatment. Due to the presence of a  $d^{10}$  configuration, pristine  $\text{CaSnO}_3$  is assumed to exhibit diamagnetic behavior.<sup>37</sup> The experimental results revealed that samples subjected to SC  $\text{CO}_2$  treatment demonstrated



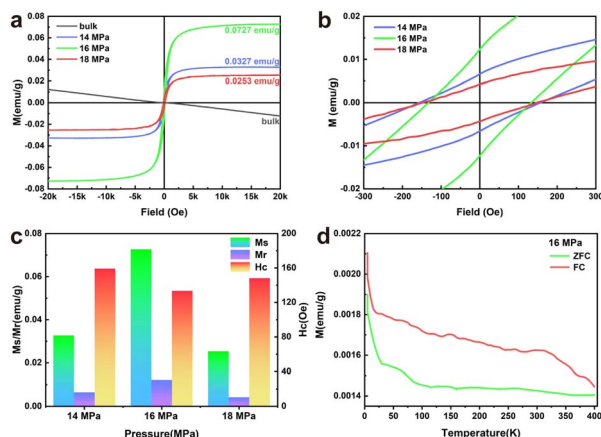


Fig. 5 Ferromagnetic behavior. (a) M–H curves at 300 K. (b) The M–H curves near  $H = 0$ . (c) Bar graph showing specific magnetic parameters. (d) FC–ZFC magnetization curve obtained at 16 MPa in an external magnetic field of 500 Oe.

pronounced magnetic ordering, with ferromagnetic properties displaying marked variations depending on the applied  $\text{CO}_2$  pressure during processing. The saturation magnetization intensity of  $\text{CaSnO}_3$  was observed to increase to 0.0327, 0.0727, and 0.0253  $\text{emu g}^{-1}$  at  $\text{CO}_2$  pressures of 14, 16, and 18 MPa, respectively. At a pressure of 16 MPa, the sample achieves the highest saturation magnetization and also reaches a maximum residual magnetization of 0.0122  $\text{emu g}^{-1}$ . Furthermore, this saturation magnetization intensity is higher than that observed for  $\text{CaSn}_{1-x}\text{Mn}_x\text{O}_3$  with  $x = 0.1$ .<sup>18</sup> Therefore, SC  $\text{CO}_2$  exhibited a remarkable ability to modulate ferromagnetism during the treatment of  $\text{CaSnO}_3$ . As illustrated in Fig. 5d, the field cooling–zero magnetic field cooling (FC–ZFC) curve of  $\text{CaSnO}_3$  treated at 16 MPa exhibits non-overlapping behavior below 400 K. This indicates that the Curie temperature after SC  $\text{CO}_2$  treatment has exceeded 400 K, demonstrating that  $\text{CaSnO}_3$  treated with SC  $\text{CO}_2$  can maintain ferromagnetic properties at temperatures above room temperature. The 16 MPa sample demonstrates a notably enhanced Curie temperature ( $T_c$ ) compared to the ZFC curves of  $\text{CaSnO}_3$  treated at 14 and 18 MPa (see Fig. S6, SI). This enhancement likely originates from an increased propensity for structural phase transitions and a higher cubic phase fraction under the 16 MPa conditions. The cubic phase, characterized by its superior symmetry and optimized bond angles for effective magnetic exchange interactions, promotes the establishment of long-range magnetic ordering. Furthermore, its inherently stronger magnetic coupling strength compared to lower-symmetry phases culminates in an elevated  $T_c$  at this specific pressure.

## Experimental

### Materials

$\text{CaSnO}_3$  (99.9%) powder was purchased from Shanghai Aladdin Biochemical Technology Co., Ltd. It was used directly, without further purification.  $\text{CO}_2$  of 99.99% purity was purchased from Henan Yuanzheng Special Gas Co. Ltd.

### $\text{CO}_2$ -induced phase engineering

50.0 mg of pure  $\text{CaSnO}_3$  powder was directly transferred into the supercritical  $\text{CO}_2$  apparatus, composed mainly of a stainless-steel autoclave with a heating jacket and a temperature controller. The autoclave was heated to the designated temperature (100 °C), and then  $\text{CO}_2$  was charged into the reactor to the desired pressure (14/16/18 MPa) and maintained for 4 h under continual stirring. After the reactor had cooled,  $\text{CO}_2$  was slowly released and the solid product  $\text{CaSnO}_3$  was collected. Finally, the samples were dried in an oven at 80 °C.

### Characterization

X-ray diffraction (XRD) patterns were collected on a Rigaku SmartLab SE diffractometer (Japan) using Cu K radiation. Transmission electron microscope (TEM) images were recorded on a JEOL JEM-F200 (Japan) at an acceleration voltage of 200 kV. Scanning electron microscope (SEM) and energy dispersive spectrometer (EDS) images were recorded on a ZEISS Sigma 360 (Germany). Raman measurements were performed using a Horiba LabRAM HR Evolution (Japan) with a laser wavelength of 532 nm. X-ray photoelectron spectroscopy (XPS) was performed using a Thermo Scientific K-Alpha system (America). The electron paramagnetic resonances (EPR) were obtained using an electron paramagnetic resonance spectrometer (EMX-9.5/12). Vibrating sample magnetometry (VSM) was performed using the LakeShore 7404 system (America). Field cooling–zero magnetic field cooling (FC–ZFC) curves were obtained using the Physical Characterisation Measurement System (China Quantum Design, PPMS-9).

## Conclusions

In summary, SC  $\text{CO}_2$  treatment successfully alters the internal chemical environment of  $\text{CaSnO}_3$ , enabling room-temperature ferromagnetism without the addition of magnetic elements. Experimental studies have demonstrated the critical synergistic role of SC  $\text{CO}_2$ -induced defect engineering and strain effects in ferromagnetic manipulation. Specifically, EPR and XPS results confirm the existence of oxygen vacancies and  $\text{Sn}^{3+}$ , directly showing that SC  $\text{CO}_2$  treatment introduces controllable lattice-scale defects in  $\text{CaSnO}_3$ , thereby releasing residual force within distorted  $\text{SnO}_6$  octahedra. This stress relaxation suppresses octahedral distortion and drives a structural phase transition from orthorhombic to cubic, as unambiguously validated by XRD, TEM and SAED characterizations. The symmetry enhancement is accompanied by anisotropic lattice expansion and tensile strain, which lowers the oxygen vacancy formation energy, consequently disrupting the intrinsic anti-ferromagnetic order and promoting ferromagnetic coupling to achieve room-temperature ferromagnetic ordering. Beyond proposing a novel non-stoichiometric doping strategy for magnetic modulation, which is a universally applicable methodology that advances the design of room-temperature magnetic functional materials, this work elucidates a defect-strain synergy mechanism capable of tuning material magnetic order, offering a transformative pathway for



developing novel functional materials for next-generation spintronic devices.

## Author contributions

L. Xu conducted experiments, collected data and wrote the original draft. Q. Xu and B. Han designed the project and funded it, and also conducted writing – review and editing.

## Conflicts of interest

There are no conflicts to declare.

## Data availability

Data for this article are available from the corresponding authors upon reasonable request.

The data supporting this article have been included as part of the supplementary information (SI). Supplementary information: supplementary structural and microstructural characterization data, including refined XRD lattice parameters, Rietveld-refined patterns, TEM and SEM images, EDS elemental analysis, total spectrum of XPS characterization, and FC-ZFC magnetization curves. See DOI: <https://doi.org/10.1039/d5sc04873g>.

## Acknowledgements

We are grateful to the National Natural Science Foundation of China (no. 51173170, 21703207, 21773216), the joint project from the Henan-Provincial and the China-National Natural Science Foundation (project no. U2004208), and the Central Plains Science and Technology Innovation Leading Talent Project (project no. 234200510008).

## Notes and references

- C. C. Mayorga-Martinez, J. Zelenka, K. Klima, P. Mayorga-Burrezo, L. Hoang, T. Ruml and M. Pumera, *ACS Nano*, 2022, **16**, 8694–8703.
- J. Lu, J. He, G. Kang, B. Lan, J. Liu and M. Zhu, *Tribol. Int.*, 2025, **202**, 110305.
- J. Chu, Y. Wang, X. Wang, K. Hu, G. Rao, C. Gong, C. Wu, H. Hong, X. Wang, K. Liu, C. Gao and J. Xiong, *Adv. Mater.*, 2020, **33**, 2004469.
- Z. Zhang, R. Sun and Z. Wang, *ACS Nano*, 2025, **19**, 187–228.
- H. M. Mohamed, I. A. Mabrouk, S. M. Yakout, Y. K. Abdel-Monem and W. Sharmoukh, *Ceram. Int.*, 2025, **51**, 1682–1689.
- W. Sharmoukh, T. A. Hameed and S. M. Yakout, *J. Alloys Compd.*, 2022, **925**, 166702.
- W. Sharmoukh and S. M. Yakout, *J. Alloys Compd.*, 2024, **993**, 174664.
- C. Sun, J. A. Alonso and J. Bian, *Adv. Energy Mater.*, 2021, **11**, 2000459.
- J. Yan, S. Zhang, Q. Wei, S. Cao, J. Zhao, B. Zou and R. Zeng, *Adv. Opt. Mater.*, 2022, **10**, 2101406.
- A. G. Ricciardulli, S. Yang, J. H. Smet and M. Saliba, *Nat. Mater.*, 2021, **20**, 1325–1336.
- J. Wang, C. Zhang, H. Liu, R. McLaughlin, Y. Zhai, S. R. Vardeny, X. Liu, S. McGill, D. Semenov, H. Guo, R. Tsuchikawa, V. V. Deshpande, D. Sun and Z. V. Vardeny, *Nat. Commun.*, 2019, **10**, 129.
- C. Zheng and Q. Liu, *RSC Adv.*, 2019, **9**, 33596–33601.
- Q. Liu, F. Jin, B. Li and L. Geng, *J. Alloys Compd.*, 2017, **717**, 55–61.
- Y. Wang, W. Lei, S. Wu, F. Niu, Q. He, Y. Shen and F. Li, *Ceram. Int.*, 2023, **49**, 14426–14431.
- S. Wi, M. Jeong, K. Lee and Y. Lee, *Adv. Sci.*, 2024, **11**, 2402848.
- A. Manoharan, M. Munusamy, A. Pradeep, S. Sellaiyan, S. Hussain and S. Krishnan, *Appl. Phys. A*, 2020, **126**, 874.
- S. Sumithra and N. Victor Jaya, *Mater. Res. Innov.*, 2019, **23**, 375–384.
- A. A. Bhat and R. Tomar, *J. Alloys Compd.*, 2021, **876**, 160043.
- Y. Ouyang, B. Gao, Y. Tang, L. Li and Q. Xu, *Chem. Sci.*, 2025, **16**, 1336–1343.
- D. Fu, M. Tan, Y. Liang and Q. Xu, *Small*, 2025, 2411243, DOI: [10.1002/smll.202411243](https://doi.org/10.1002/smll.202411243).
- W. Liu, Q. Xu, W. Cui, C. Zhu and Y. Qi, *Angew. Chem., Int. Ed.*, 2017, **56**, 1600–1604.
- Y. Zhou, Q. Xu, T. Ge, X. Zheng, L. Zhang and P. Yan, *Angew. Chem., Int. Ed.*, 2020, **59**, 3322–3328.
- B. Gao, S. Xu and Q. Xu, *Angew. Chem., Int. Ed.*, 2022, **61**, e202117084.
- T. Ge, W. Cui and Q. Xu, *Angew. Chem., Int. Ed.*, 2023, **62**, e202300446.
- Y. Zhou, P. Yan, J. Jia, S. Zhang, X. Zheng, L. Zhang, B. Zhang, J. Chen, W. Hao, G. Chen, Q. Xu and B. Han, *J. Mater. Chem. A*, 2020, **8**, 13320–13327.
- L. Du, B. Gao, S. Xu and Q. Xu, *Nat. Commun.*, 2023, **14**, 2278.
- Ž. Knez, E. Markočič, M. Leitgeb, M. Primožič, M. Knez Hrnčič and M. Škerget, *Energy*, 2014, **77**, 235–243.
- H. Shaili, E. Salmani, M. Beraich, M. Zidane, M. Taibi, M. Rouchdi, H. Ez-Zahraouy, N. Hassanain and A. Mzerd, *ACS Omega*, 2021, **6**, 32537–32547.
- H. P. Rooksby, *Nature*, 1945, **155**, 484.
- J. Gao, H. Zhang, L. Xie, J. Yu, G. Wang, Y. Gu, H. He and J. Bai, *J. Eur. Ceram. Soc.*, 2017, **37**, 985–994.
- H. L. Zheng, Z. C. Zhang, J. G. Zhou, S. S. Yang and J. Zhao, *Appl. Phys. A*, 2012, **108**, 465–473.
- J. Kung, Y.-J. Lin and C.-M. Lin, *J. Chem. Phys.*, 2011, **135**, 224507.
- M. D. Williams, D. S. Bradshaw and D. L. Andrews, *J. Chem. Phys.*, 2016, **145**, 184301.
- C. Zhang, R. Lu, C. Liu, L. Yuan, J. Wang, Y. Zhao and C. Yu, *Adv. Funct. Mater.*, 2021, **31**, 2100099.
- J. Liu, Y. Xiang, Y. Chen, H. Zhang, B. Ye, L. Ren, W. Tan, A. Kappler and J. Hou, *Environ. Sci. Technol.*, 2023, **57**, 12453–12464.
- X. Song, H. Ma, Y. Li, Y. Duan, W. Wang and F. Dong, *Appl. Catal., B*, 2025, **365**, 124955.
- A. Manoharan, B. Suresh, k. Ajay, M. Munisamy and S. Krishnan, *Solid State Commun.*, 2023, **360**, 115033.

